Free vibration analysis of functionally graded plates using the element-free *kp*-Ritz method

X. Zhao, Y.Y. Lee, K.M. Liew*

Department of Building and Construction, City University of Hong Kong, Tat Chee Avenue, Kowloon, Hong Kong

Abstract

A free vibration analysis of metal and ceramic functionally graded plates that uses the element-free *kp*-Ritz method is presented. The material properties of the plates are assumed to vary continuously through their thickness according to a power-law distribution of the volume fractions of the plate constituents. The first-order shear deformation plate theory is employed to account for the transverse shear strain and rotary inertia, and mesh-free kernel particle functions are used to approximate the two-dimensional displacement fields. The eigen-equation is obtained by applying the Ritz procedure to the energy functional of the system. Convergence studies are performed to examine the stability of the proposed method, and comparisons of the solutions derived with those reported in the literature are provided to verify its accuracy. Four types of functionally graded rectangular and skew plates—Al/Al$_2$O$_3$, Al/ZrO$_2$, Ti–6Al–4V/Aluminum oxide, and SUS304/Si$_3$N$_4$—are included in the study, and the effects of the volume fraction, boundary conditions, and length-to-thickness ratio on their frequency characteristics are discussed in detail.

© 2008 Elsevier Ltd. All rights reserved.

1. Introduction

Functionally graded materials (FGMs) are special composites with material properties that vary continuously through their thickness. FGMs are usually made of a mixture of ceramic and metal, and can thus resist high-temperature conditions while maintaining toughness. The primary applications of FGMs are in high-temperature environments, but the scope of their application is expanding.

Since the concept of FGMs [1] was first proposed, FGMs have been extensively studied by researchers, who have mainly focused on their thermo-elastic behavior. Noda [2] provided a comprehensive discussion of thermal stress in FGMs subjected to a steady-temperature field or thermal shock, and Praveen and Reddy [3] investigated the static and dynamic thermo-elastic response of functionally graded plates (FGPs) using the finite element method. Liew et al. [4,5] studied the thermal post-buckling of FGPs with temperature-dependent properties and the post-buckling of piezoelectric FGM plates subject to thermo-electro-mechanical loading. Reddy [6] presented a theoretical formulation and finite element models for FGPs based on the third-order

---

*Corresponding author.

E-mail address: kmliew@cityu.edu.hk (K.M. Liew).

shear deformation theory. The formulations accounted for the thermomechanical coupling, time dependency, and von Kármán-type geometric nonlinearity of the plates. Other work on FGMs has investigated three-dimensional solutions for smart FGPs [7], the optimal shape control of FGPS [8,9], the modelling and design of smart structures using FGMs and piezoelectric sensor/actuator patches [10], and the thermal stress behavior of functional graded hollow circular cylinders [11].

Researchers have also turned their attention to the vibration and dynamic response of functionally graded structures [12–14]. Sheng and Wang [15] investigated the effect of thermal load on vibration, buckling and dynamic stability of functionally graded cylindrical shells embedded in an elastic medium. He et al. [16] presented a finite element formulation for the shape and vibration control of FGPs with integrated piezoelectric sensors and actuators, and investigated the effects of the volume fractions of the constituents on the dynamic response of Aluminum oxide/Ti–6Al–4V FGM plates. Using a semi-analytical approach, Yang and Shen [17] studied the free vibration and dynamic response of FGPs subjected to impulsive lateral loads combined with initial in-plane actions in a thermal environment. A three-dimensional solution for the free and forced vibration of simply supported FGPs was provided by Vel and Batra [18] using different plate theories, and Liew et al. [19] carried out the Finite element piezothermoelasticity analysis and the active control of FGM plates with integrated piezoelectric sensors and actuators. The frequency characteristics of thick annular FGPs of variable thickness were analyzed by Efraim and Eisenberger [20], who utilized the first-order shear deformation theory and exact element method to derive the stiffness matrix. Recently, Matsunaga [21] carried out an analysis of the free vibration and stability of FGPs using the two-dimensional higher-order deformation theory.

Mesh-free methods developed in recent years have been widely applied in a variety of engineering problems. The element-free Galerkin method was used for the analysis of thin plates and shells [22,23], the pseudoelastic behavior analysis of a SMA beam [24], the buckling analysis of corrugated plates [25], free vibration analysis of fold plates [26]. The other notable mesh-free methods include the reproducing kernel particle method [27–29] and the meshless local Petrov–Galerkin method [30].

This study presents a method for analyzing the free vibration of FGPs with arbitrary boundary conditions using the element-free kp-Ritz method, which has already been successfully applied to the analysis of isotropic and composite structures [31–34]. The first-order shear deformation plate theory is used to take account into the transverse shear deformation. The elastic properties of the FGPs are determined by the volume fractions of their constituents, which vary continuously through their thickness according to a power law. The bending stiffness and the shear stiffness are separately computed; the bending stiffness is estimated by using the full Gauss integration, whereas the shear stiffness is evaluated by using the one-point gauss point integration in order to avoid the shear locking. Convergence studies and comparisons are provided to verify the stability and accuracy of the method in analyzing four types of FGPs: Al/Al$_2$O$_3$, Al/ZrO$_2$, Ti–6Al–4V/Aluminum oxide, and SUS304/Si$_3$N$_4$. The influences of the boundary conditions, volume fraction exponent, and length-to-thickness ratio on the frequency characteristics of FGPs are also examined in detail.

2. Functionally graded material properties

A functionally graded plate (shown in Fig. 1) is considered to be a single-layered plate of uniform thickness that is made of ceramic and metal. The material property is assumed to be graded through the thickness in accordance with a power-law distribution that is expressed as

$$P(z) = (P_c - P_m)V_c + P_m, \tag{1a}$$

$$V_c = \left(\frac{1}{2} + \frac{z}{h}\right)^n \quad (n \geqslant 0), \tag{1b}$$

where P represents the effective material property, P_c and P_m denote the properties of the ceramic and metal, respectively, V_c is the volume fraction of the ceramic, h is the thickness of the plate, and n is the volume fraction exponent. Fig. 2 shows the variation of the volume fraction through the thickness for different exponents n. The effective material properties of the plate, including Young's modulus E, density ρ, Poisson ratio v, and thermal expansion β, vary according to Eq. (1). The properties of the temperature-dependent
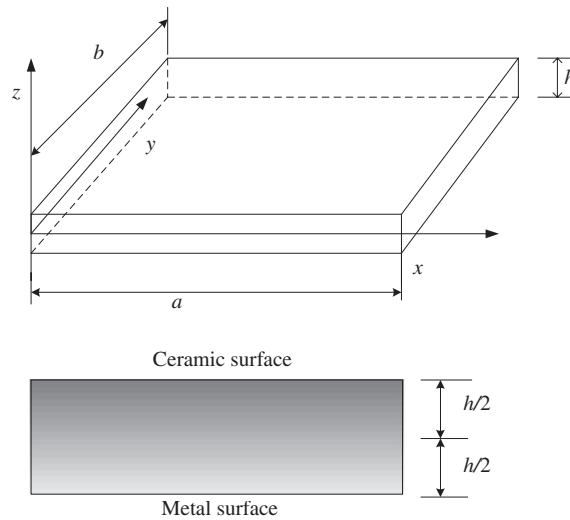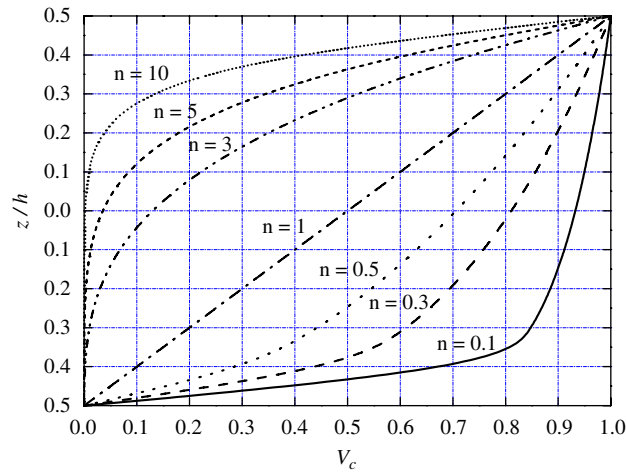
Fig. 1. Functionally graded plate.

Fig. 2. Variation of the volume fraction V_c through the thickness.

constituents of FGPs, such as Ti–6Al–4V, silicon nitride (Si_3N_4) and stainless steel (SUS304), can be expressed as a nonlinear function of temperature [35] as

$$P = P_0(P_{-1}T^{-1} + 1 + P_1T + P_2T^2 + P_3T^3), \tag{2}$$

where P_0, P_{-1}, P_1, P_2, and P_3 are the coefficients of temperature T. The values of the coefficients for Ti–6Al–4V and Aluminum oxide are given in Table 1 as an example [36].

3. Theoretical formulations

3.1. Energy functional

According to the first-order shear deformation plate theory [37], the displacement field can be expressed as

$$u(x, y, z) = u_0(x, y) + z\theta_x(x, y),$$
$$v(x, y, z) = v_0(x, y) + z\theta_y(x, y),$$
$$w(x, y, z) = w_0(x, y), \tag{3}$$

Table 1
Material constants of Ti–6Al–4V and Aluminum oxide

Material constant	Aluminum oxide			Ti–6Al–4V		
	E (N/m^2)	v	ρ (kg/m^3)	E (N/m^2)	v	ρ (kg/m^3)
P_0	349.55×10^9	0.26	3750	122.56×10^9	0.2884	4429
P_{-1}	0	0	0	0	0	0
P_1	-3.853×10^{-4}	0	0	-4.586×10^{-4}	1.12×10^{-4}	0
P_2	4.027×10^{-7}	0	0	0	0	0
P_3	-1.673×10^{-10}	0	0	0	0	0
P	3.2024×10^{11}	0.26	3750	1.057×10^{11}	0.2981	4429

where u_0, v_0, and w_0 denote the displacements of the mid-plane of the plate in the x, y, and z directions, and θ_x and θ_y represent the rotations of the transverse normal about the y- and x-axis, respectively.

The linear strains are given by

$$\left\{ \begin{array}{c} \varepsilon_{xx} \\ \varepsilon_{yy} \\ \gamma_{xy} \end{array} \right\} = \left\{ \begin{array}{c} \dfrac{\partial u_0}{\partial x} \\ \dfrac{\partial v_0}{\partial y} \\ \dfrac{\partial u_0}{\partial y} + \dfrac{\partial v_0}{\partial x} \end{array} \right\} + z \left\{ \begin{array}{c} \dfrac{\partial \theta_x}{\partial x} \\ \dfrac{\partial \theta_y}{\partial y} \\ \dfrac{\partial \theta_x}{\partial y} + \dfrac{\partial \theta_y}{\partial x} \end{array} \right\} = \{\varepsilon_0\} + z\{\kappa\},$$

$$\left\{ \begin{array}{c} \gamma_{yz} \\ \gamma_{xz} \end{array} \right\} = \left\{ \begin{array}{c} \theta_y + \dfrac{\partial w_0}{\partial y} \\ \theta_x + \dfrac{\partial w_0}{\partial x} \end{array} \right\} = \{\gamma_0\}. \tag{4}$$

The strain energy of the plate is expressed by

$$U_\varepsilon = \frac{1}{2} \int_\Omega \varepsilon^{\mathrm{T}} \mathbf{S} \, \varepsilon \, \mathrm{d}\Omega, \tag{5}$$

where ε and $\mathbf{S}$ are given by

$$\varepsilon = \left\{ \begin{array}{c} \varepsilon_0 \\ \kappa \\ \gamma_0 \end{array} \right\}, \tag{6}$$

$$\mathbf{S} = \begin{bmatrix} A_{11} & A_{12} & A_{16} & B_{11} & B_{12} & B_{16} & 0 & 0 \\ A_{12} & A_{22} & A_{26} & B_{12} & B_{22} & B_{26} & 0 & 0 \\ A_{16} & A_{26} & A_{66} & B_{16} & B_{26} & B_{66} & 0 & 0 \\ B_{11} & B_{12} & B_{16} & D_{11} & D_{12} & D_{16} & 0 & 0 \\ B_{12} & B_{22} & B_{26} & D_{12} & D_{22} & D_{26} & 0 & 0 \\ B_{16} & B_{26} & B_{66} & D_{16} & D_{26} & D_{66} & 0 & 0 \\ 0 & 0 & 0 & 0 & 0 & 0 & A_{44}^s & A_{45}^s \\ 0 & 0 & 0 & 0 & 0 & 0 & A_{45}^s & A_{55}^s \end{bmatrix} = \begin{bmatrix} \mathbf{A} & \bar{\mathbf{B}} & \mathbf{0} \\ \bar{\mathbf{B}} & \mathbf{D} & \mathbf{0} \\ \mathbf{0} & \mathbf{0} & \mathbf{A}^s \end{bmatrix}, \tag{7}$$

in which the extensional A_{ij}, coupling B_{ij}, bending D_{ij}, and transverse shear A_{ij}^s stiffnesses are defined as

$$(A_{ij}, B_{ij}, D_{ij}) = \int_{-h/2}^{h/2} Q_{ij}(1, z, z^2) \, \mathrm{d}z, \quad A_{ij}^s = K \int_{-h/2}^{h/2} Q_{ij} \, \mathrm{d}z, \tag{8}$$

where A_{ij}, B_{ij}, and D_{ij} are defined for $i, j = 1,2,6$ and A_{ij}^s is defined for $i, j = 4,5$. K denotes the transverse shear correction coefficient and is taken as $K = 5/6$ for the isotropic material. The elastic coefficient Q_{ij} is given by

$$Q_{11} = \frac{E}{1 - v^2}, \quad Q_{12} = vQ_{11}, \quad Q_{22} = Q_{11}, \quad Q_{44} = Q_{55} = Q_{66} = \frac{E}{2(1 - v)}. \tag{9}$$

As Young's modulus E and Poisson ratio v vary through the thickness according to Eq. (1), the elastic coefficient Q_{ij} is a function of position z.

In the free vibration analysis of plates, the kinetic energy of the plates is given by

$$\Theta = \frac{1}{2} \int_{\Omega} \int_{-h/2}^{h/2} \rho(z)(\dot{u}^2 + \dot{v}^2 + \dot{w}^2) \, dz \, d\Omega \tag{10}$$

and the total energy functional is thus given by

$$\Pi = U_\varepsilon - \Theta. \tag{11}$$

3.2. Two-dimensional kernel particle shape functions

Consider an approximation of function $u(\mathbf{x})$ that is denoted by u^h and expressed in discrete form as

$$u^h = \sum_{I=1}^{NP} \psi_I(\mathbf{x})\mathbf{u}_I, \tag{12}$$

where NP is the number of nodes, and $\psi_I(\mathbf{x})$ and $\mathbf{u}_I$ are the shape function and coefficient associated with node I.

The construction of the shape functions is based on the kernel particle concept [27,28]. A two-dimensional shape function is given by

$$\psi_I(\mathbf{x}) = C(\mathbf{x})\Phi_a(\mathbf{x} - \mathbf{x}_I), \tag{13}$$

where $\Phi_a(\mathbf{x} - \mathbf{x}_I)$ is termed a kernel function with compact support and $C(\mathbf{x})$ is termed a correction function, which is used to satisfy the reproducing condition

$$\sum_{I=1}^{NP} \psi_I(\mathbf{x})x_I^p y_I^q = x^p y^q \quad \text{for} \quad p + q = 0, 1, 2. \tag{14}$$

The correction function $C(\mathbf{x})$ is described as a linear combination of the complete second-order monomial functions

$$C(\mathbf{x}) = \mathbf{H}^{\mathrm{T}}(\mathbf{x} - \mathbf{x}_I)\mathbf{b}(\mathbf{x}), \tag{15}$$

$$\mathbf{b}(\mathbf{x}) = [b_0(x,y), b_1(x,y), b_2(x,y), b_3(x,y), b_4(x,y), b_5(x,y)]^{\mathrm{T}}, \tag{16}$$

$$\mathbf{H}^{\mathrm{T}}(\mathbf{x} - \mathbf{x}_I) = [1, x - x_I, y - y_I, (x - x_I)(y - y_I), (x - x_I)^2, (y - y_I)^2], \tag{17}$$

where $\mathbf{H}$ is a vector of the quadratic basis and $\mathbf{b}(\mathbf{x})$ is a vector that is determined later. The shape function can therefore be written as

$$\psi_I(\mathbf{x}) = \mathbf{b}^{\mathrm{T}}(\mathbf{x})\mathbf{H}(\mathbf{x} - \mathbf{x}_I)\Phi_a(\mathbf{x} - \mathbf{x}_I). \tag{18}$$

Eq. (18) can be rewritten as

$$\psi_I(\mathbf{x}) = \mathbf{b}^{\mathrm{T}}(\mathbf{x})\mathbf{B}_I(\mathbf{x} - \mathbf{x}_I), \tag{19}$$

where

$$\mathbf{B}_I(\mathbf{x} - \mathbf{x}_I) = \mathbf{H}(\mathbf{x} - \mathbf{x}_I)\Phi_a(\mathbf{x} - \mathbf{x}_I). \tag{20}$$

The coefficients $\mathbf{b}(\mathbf{x})$ can be solved by substituting Eq. (19) into Eq. (14)

$$\mathbf{b}(\mathbf{x}) = \mathbf{M}^{-1}(\mathbf{x})\mathbf{H}(\mathbf{0}), \tag{21}$$

where $\mathbf{M}$ is the moment matrix and $\mathbf{H}(0)$ is a constant vector. The expressions for $\mathbf{M}$ and $\mathbf{H}(0)$ are given by

$$\mathbf{M}(\boldsymbol{x}) = \sum_{I=1}^{NP} \mathbf{H}(\boldsymbol{x} - \boldsymbol{x}_I)\mathbf{H}^{\mathrm{T}}(\boldsymbol{x} - \boldsymbol{x}_I)\Phi_a(\boldsymbol{x} - \boldsymbol{x}_I),$$

$$\mathbf{H}(0) = [1, 0, 0, 0, 0, 0]^{\mathrm{T}}. \tag{22}$$

For a two-dimensional problem, the kernel function $\Phi_a(\boldsymbol{x}-\boldsymbol{x}_I)$ is expressed as

$$\Phi_a(\boldsymbol{x} - \boldsymbol{x}_I) = \Phi_a(x)\Phi_a(y), \tag{23}$$

in which

$$\Phi_a(x) = \phi\left(\frac{x - x_I}{a}\right), \tag{24}$$

where $\phi(x)$ is the weight function. The cubic spline function is chosen as the weight function, and is given by

$$\phi_z(z_I) = \begin{cases} \frac{2}{3} - 4z_I^2 + 4z_I^3 & \text{for} & 0 \leqslant |z_I| \leqslant \frac{1}{2} \\ \frac{4}{3} - 4z_I + 4z_I^2 - \frac{4}{3}z_I^3 & \text{for} & \frac{1}{2} < |z_I| \leqslant 1 \\ 0 & \text{otherwise} \end{cases}$$

$$z_I = \frac{(x - x_I)}{d_I}, \tag{25}$$

where the dilatation parameter d_I is the size of the support. The size of the domain of influence at a node is calculated by

$$d_I = d_{\max}c_I, \tag{26}$$

where $d_{\max}$ is a scaling factor. The distance c_I is determined by searching for a sufficient number of nodes that avoids the singularity of the matrix $\mathbf{M}$. The number of nodes should not be less than six for a quadratic basis, as otherwise the matrix $\mathbf{M}$ will not be invertible.

The shape function can therefore be expressed as

$$\psi_I(\boldsymbol{x}) = \mathbf{H}^{\mathrm{T}}(0)\mathbf{M}^{-1}(\boldsymbol{x})\mathbf{H}(\boldsymbol{x} - \boldsymbol{x}_I)\Phi_a(\boldsymbol{x} - \boldsymbol{x}_I). \tag{27}$$

As the shape function $\psi_I(\boldsymbol{x})$ does not possess Kronecker delta properties, the boundary conditions cannot be directly imposed. Several methods, such as the transformation method [27], Lagrange multipliers [38], and the penalty method, have been proposed to impose the essential boundary conditions.

3.3. Discrete eigen-equation

For a plate discretized by a set of nodes $\boldsymbol{x}_I$, $I = 1, \ldots, NP$, which are the discrete displacement approximations of the mid-plane, are expressed as

$$\mathbf{u}_0^h = \begin{pmatrix} u_0^h \\ v_0^h \\ w_0^h \\ \theta_x^h \\ \theta_y^h \end{pmatrix} = \sum_{I=1}^{NP} \psi_I \begin{pmatrix} u_I \\ v_I \\ w_I \\ \theta_{xI} \\ \theta_{yI} \end{pmatrix} \mathrm{e}^{\mathrm{i}\omega t} = \sum_{I=1}^{NP} \psi_I(\boldsymbol{x})\mathbf{u}_I\, \mathrm{e}^{\mathrm{i}\omega t}. \tag{28}$$

Substituting Eq. (28) into Eq. (11) and taking the variation in the energy functional yields the eigen-equation

$$(\tilde{\mathbf{K}} - \omega^2\tilde{\mathbf{M}})\tilde{\mathbf{u}} = 0, \tag{29}$$

where

$$\tilde{\mathbf{K}} = \boldsymbol{\Lambda}^{-1}\mathbf{K}\boldsymbol{\Lambda}^{-\mathrm{T}}, \quad \tilde{\mathbf{M}} = \boldsymbol{\Lambda}^{-1}\bar{\mathbf{M}}, \quad \tilde{\mathbf{u}} = \boldsymbol{\Lambda}\mathbf{u} \tag{30}$$

$$\mathbf{\Lambda}_{IJ} = \psi_I(x_J)\mathbf{I}, \quad \mathbf{I} \text{ is the identity matrix} \tag{31}$$

$$\mathbf{K} = \mathbf{K}^b + \mathbf{K}^m + \mathbf{K}^s, \tag{32}$$

$$\mathbf{K}_{IJ}^b = \int_{\Omega} \mathbf{B}_I^{b^{\mathrm{T}}} \mathbf{D} \mathbf{B}_J^b \, \mathrm{d}\Omega, \tag{33}$$

$$\mathbf{K}_{IJ}^m = \int_{\Omega} \mathbf{B}_I^{m^{\mathrm{T}}} \mathbf{A} \mathbf{B}_J^m \, \mathrm{d}\Omega + \int_{\Omega} \mathbf{B}_I^{m^{\mathrm{T}}} \mathbf{B} \mathbf{B}_J^b \, \mathrm{d}\Omega + \int_{\Omega} \mathbf{B}_I^{b^{\mathrm{T}}} \mathbf{B} \mathbf{B}_J^m \, \mathrm{d}\Omega, \tag{34}$$

$$\mathbf{K}_{IJ}^s = \int_{\Omega} \mathbf{B}_I^{s^{\mathrm{T}}} \mathbf{A}^s \mathbf{B}_J^s \, \mathrm{d}\Omega, \tag{35}$$

$$\bar{\mathbf{M}}_{IJ} = \int_{\Omega} \mathbf{G}_I^{\mathrm{T}} \bar{\mathbf{m}} \, \mathbf{G}_J \, \mathrm{d}\Omega, \tag{36}$$

$$\mathbf{B}_I^b = \begin{bmatrix} 0 & 0 & 0 & \dfrac{\partial \psi_I}{\partial x} & 0 \\[2mm] 0 & 0 & 0 & 0 & \dfrac{\partial \psi_I}{\partial y} \\[2mm] 0 & 0 & 0 & \dfrac{\partial \psi_I}{\partial y} & \dfrac{\partial \psi_I}{\partial x} \end{bmatrix}, \quad \mathbf{B}_I^m = \begin{bmatrix} \dfrac{\partial \psi_I}{\partial x} & 0 & 0 & 0 & 0 \\[2mm] 0 & \dfrac{\partial \psi_I}{\partial y} & 0 & 0 & 0 \\[2mm] \dfrac{\partial \psi_I}{\partial y} & \dfrac{\partial \psi_I}{\partial x} & 0 & 0 & 0 \end{bmatrix}, \tag{37}$$

$$\mathbf{B}_I^s = \begin{bmatrix} 0 & 0 & \dfrac{\partial \psi_I}{\partial x} & \psi_I & 0 \\[2mm] 0 & 0 & \dfrac{\partial \psi_I}{\partial y} & 0 & \psi_I \end{bmatrix}, \quad \mathbf{G}_I = \begin{bmatrix} \psi_I & 0 & 0 & 0 & 0 \\ 0 & \psi_I & 0 & 0 & 0 \\ 0 & 0 & \psi_I & 0 & 0 \\ 0 & 0 & 0 & \psi_I & 0 \\ 0 & 0 & 0 & 0 & \psi_I \end{bmatrix}, \tag{38}$$

$$\bar{\mathbf{m}} = \begin{bmatrix} I_0 & 0 & 0 & I_1 & 0 \\ 0 & I_0 & 0 & 0 & I_1 \\ 0 & 0 & I_0 & 0 & 0 \\ I_1 & 0 & 0 & I_2 & 0 \\ 0 & I_1 & 0 & 0 & I_2 \end{bmatrix} \quad (I_0, I_1, I_2) = \int_{-h/2}^{h/2} \rho(z)(1, z, z^2) \, \mathrm{d}z, \tag{39}$$

where the density $\rho(z)$ is determined by Eq. (1). The matrices $\mathbf{A}$, $\bar{\mathbf{B}}$, $\mathbf{D}$, and $\bar{\mathbf{m}}$ can be computed using either an analytical or a numerical method. If the constituents of the FGPs have different Poisson ratios, then analytical forms of matrices $\mathbf{A}$, $\bar{\mathbf{B}}$, $\mathbf{D}$ may not always exist, and it is for this reason that a recursive adaptive Simpson quadrature is employed here to calculate the matrices. The matrices $\mathbf{K}^b$, $\mathbf{K}^m$, $\mathbf{K}^s$ and $\bar{\mathbf{M}}$ are evaluated using the Gauss integration method.

4. Numerical results

The properties of the temperature-dependent constituents of FGPs are calculated according to Eq. (2). Table 1 shows the corresponding material constants of Aluminum oxide and Ti–6Al–4V, and Fig. 3 shows the plots of the variation with temperature of Young's modulus E for four types of material—Aluminum oxide, Ti–6Al–4V, SUS304 and Si$_3$N$_4$—with the values of Young's modulus for Ti–6Al–4V and SUS304 being represented on the right vertical axis. A distinctive relationship between Young's modulus and the temperature can be observed for each material. The properties of the constituents of the FGPs are given at temperature $T = 300$ K (room temperature) unless specified otherwise. The kernel particle function is employed to construct approximations of the two-dimensional displacement field. A scaling factor that represents the size
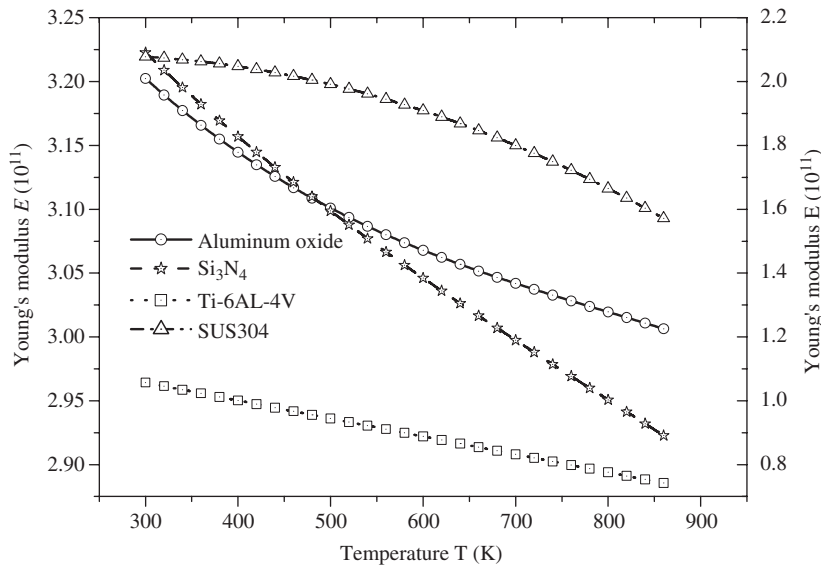
Fig. 3. Variation of Young's modulus with temperature for different materials.

Table 2
Properties of the FGM components

Material	Properties		
	E (N/m^2)	v	ρ (kg/m^3)
Aluminum (Al)	70.0×10^9	0.30	2707
Alumina (Al$_2$O$_3$)	380×10^9	0.30	3800
Zirconia(ZrO$_2$)	151×10^9	0.30	3000
Ti–Al–4V	105.7×10^9	0.298	4429
Aluminum oxide	320.2×10^9	0.26	3750
Stainless steel SUS304	207.78×10^9	0.3177	8166
Silicon nitride Si$_3$N$_4$	322.27×10^9	0.24	2370

of the support of 3.0 is used, and a background cell structure based on the nodes is generated to perform the numerical integration. A 4×4 Gauss integration is used to compute the bending stiffness $\mathbf{K}^b$ and coupling stiffness $\mathbf{K}^m$, and the shear stiffness $\mathbf{K}^s$ is evaluated with a one-point Gauss integration. The transformation method is employed to impose the essential boundary conditions.

4.1. Convergence study

To verify the results, the convergence properties of simply supported square FGPs are examined in terms of the number of nodes required. The plates consist of Aluminum (Al) and Alumina (Al$_2$O$_3$), the properties of which are given in Table 2. Plates with the length-to-thickness ratios $a/h = 5$ and 10 are considered, and the values of the volume fraction exponent are taken to be $n = 0, 0.5, 1, 4, 10$. The fundamental natural frequency parameter $\bar{\omega} = \omega h \sqrt{\rho_c / E_c}$, as provided in Table 3, is compared with the solutions reported by Matsunaga [21] using a higher-order deformation theory. It is found that the results of this study show a trend of monotonic convergence trend, and that the solutions are slightly larger than those given in the literature. The difference ranges from 1.4% to 2% for the plates with $a/h = 10$, and from 1.6% to 3.4% for the plates with $a/h = 5$. The maximum difference occurs when $a/h = 5$ and $n = 0.5$. These discrepancies may be due to the different plate theories adopted and the solution strategies used in the two studies.

Table 3
Comparison of the natural frequency parameter $\bar{\omega} = \omega h \sqrt{\rho_c / E_c}$ for simply supported square Al/Al$_2$O$_3$ FG plates

a/h	n				
	0	0.5	1	4	10
5					
Present					
9×9	0.2018	0.1726	0.1559	0.1332	0.1261
11×11	0.2035	0.1740	0.1572	0.1343	0.1271
13×13	0.2045	0.1748	0.1579	0.1349	0.1277
15×15	0.2051	0.1753	0.1584	0.1354	0.1281
17×17	0.2055	0.1757	0.1587	0.1356	0.1284
Matsunaga [21]	0.2121	0.1819	0.1640	0.1383	0.1306
10					
Present					
9×9	0.05606	0.04763	0.04296	0.03712	0.03547
11×11	0.05632	0.04783	0.04315	0.03729	0.03564
13×13	0.05649	0.04799	0.04328	0.03741	0.03576
15×15	0.05663	0.04809	0.04338	0.03750	0.03585
17×17	0.05673	0.04818	0.04346	0.03757	0.03591
Matsunaga [21]	0.05777	0.04917	0.04426	0.03811	0.03642

Table 4
Comparison of the natural frequency ω (Hz) for simply supported square Ti–Al–4V/Aluminum oxide FG plates ($a = b = 0.4$, $h = 0.005$)

Mode	$n = 0$			$n = 2000$		
	Present	Bishop [39]	He et al. [16]	Present	Bishop [39]	He et al. [16]
1	143.67	145.04	144.66	268.60	271.23	268.92
2	360.64	362.61	360.53	674.38	678.06	669.40
3	360.64	362.61	360.53	674.38	678.06	669.40
4	575.87	580.18	569.89	1076.8	1084.9	1052.49
5	725.53	725.22	720.57	1356.9	1356.1	1338.52
6	725.53	725.22	720.57	1356.9	1356.1	1338.52
7	938.18	942.79	919.74	1754.4	1763.0	1695.23
8	938.18	942.79	919.74	1754.4	1763.0	1695.23
9	1238.76	1233.0	1225.72	2316.9	2305.4	2280.95
10	1238.76	1233.0	1225.72	2316.9	2305.4	2280.95

Table 4 shows a comparison of the natural frequencies of simply supported square FGPs derived using the method proposed here with those given by Bishop [39] and He et al. [16]. The geometric properties of the plates are $a = b = 0.4$ m, $h = 0.005$ m. The FGPs consist of Ti–6Al–4V and Aluminum oxide, the properties of which are listed in Table 2. Two special volume fraction components $n = 0$ and 2000 are selected. It can be seen that the solutions from this study agree well with those presented by Bishop [39], and also match the results reported by He et al. [16], except for a few higher modes where slightly larger differences are observed.

4.2. Square plates

In this section, the frequency characteristics of four types of square plates—Al/Al$_2$O$_3$, Al/ZrO$_2$, Ti–6Al–4V/Aluminum oxide, and SUS304/Si$_3$N$_4$—are investigated. The properties of the constituents are provided in Table 2. The volume fraction exponent n varies from 0 to 10, and the thickness of the plates is $h = 0.01$ m. The two length-to-thickness ratios $a/h = 10$ and 100 are selected, and three types of boundary conditions—all edges simply supported (SSSS), one edge clamped and the other three free (CFFF), and all edges clamped

(CCCC)—are considered. A regular 17×17 nodal distribution is chosen for the convergence studies. The simply supported boundary condition is expressed as

$$\text{At } x = 0, a: \quad v_0 = w_0 = \theta_y = 0$$
$$\text{At } y = -b/2, \, b/2: \quad u_0 = w_0 = \theta_x = 0. \tag{40}$$

The boundary conditions at the clamped edges are given by

$$u_0 = v_0 = w_0 = \theta_x = \theta_y = 0 \tag{41}$$

and the frequency parameter ω^* is defined as

$$\omega^* = \omega a^2 / h \sqrt{\rho_c / E_c}. \tag{42}$$

Table 5 shows the variation of the non-dimensional frequency parameter with the volume fraction exponent for the Al/Al_2O_3 plates ($a/h = 10$). Only the results for the first four modes are computed. For the plates with the SSSS boundary condition, the frequencies in all four modes decrease as the volume fraction exponent n increases, with the trend becoming gentler as n increases. This is expected, because a larger volume fraction exponent means that a plate has a smaller ceramic component, and that its stiffness is thus reduced. Similar trends are also observed for the CFFF and CCCC boundary conditions.

The variation of the non-dimensional frequency parameter with the volume fraction exponent for plates made of Al/ZrO_2, Ti–6Al–4V/Aluminum oxide, and $SUS304/Si_3N_4$, is described in Tables 6–8, respectively. The frequency characteristics shown in these three tables are similar to those in Table 5.

Table 9 shows the effect of the temperature on the frequency parameter ω^* for the square Ti–6Al–4V/Aluminum oxide plates ($a/h = 10$) with SSSS and CCCC boundary conditions. The temperature varies from 100 to 1000 K. It can be seen that the natural frequency declines as the temperature goes up. It is because Young's modulus is getting weaker when the temperature goes up; hence the weaker Young's modulus results in the lower natural frequency.

Fig. 4 shows a comparison of the fundamental natural frequency parameters of four simply supported plates. It can be seen that all of the curves that represent the various combinations show a similar behavior, with the frequencies dropping as the volume fraction exponent increases. The curves for the plates made of a combination of Al/Al_2O_3 and Ti–6Al–4V/Aluminum oxide nearly overlap, whereas the curve for the Al/ZrO_2 plate has the highest values and the curve for the $SUS304/Si_3N_4$ the lowest. A prominent drop in frequency occurs when the volume fraction exponent varies between 0 and 2, but after passing 5 all of the curves become flatter. Similar conclusions can be drawn from Figs. 5 and 6 for plates with the CCCC and CFFF boundary conditions.

Table 5
Variation of the frequency parameter $\omega^* = \omega a^2 / h \sqrt{\rho_c / E_c}$ with the volume fraction exponent n for square Al/Al_2O_3 FG plates ($a/h = 10$)

Boundary condition	Mode	n						
		0	0.5	1	2	5	8	10
SSSS	1	5.6763	4.8209	4.3474	3.9474	3.7218	3.6410	3.5923
	2	13.537	11.539	10.416	9.4435	8.8448	8.6264	8.5037
	3	13.537	11.539	10.416	9.4435	8.8448	8.6264	8.5037
	4	20.633	17.639	15.936	14.431	13.445	13.082	12.887
CFFF	1	1.0298	0.8728	0.7867	0.7150	0.6768	0.6633	0.6547
	2	2.3907	2.0313	1.8324	1.6639	1.5678	1.5332	1.5125
	3	6.0047	5.1061	4.6048	4.1769	3.9273	3.8382	3.7861
	4	7.6356	5.8932	5.4609	4.9331	4.2625	3.9916	3.8852
CCCC	1	9.6329	8.2388	7.4533	6.7629	6.3060	6.1314	6.0375
	2	18.313	15.742	14.265	12.924	11.946	11.567	11.377
	3	18.313	15.742	14.265	12.924	11.946	11.567	11.377
	4	25.499	21.979	19.935	18.042	16.597	16.037	15.763

Table 6
Variation of the frequency parameter $\omega^* = \omega a^2/h\sqrt{\rho_c/E_c}$ with the volume fraction exponent n for square Al/ZrO$_2$ FG plates ($a/h = 10$)

Boundary condition	Mode	n						
		0	0.5	1	2	5	8	10
SSSS	1	5.6763	5.1105	4.8713	4.6977	4.5549	4.4741	4.4323
	2	13.537	12.207	11.633	11.199	10.828	10.632	10.533
	3	13.537	12.207	11.633	11.199	10.828	10.632	10.533
	4	20.633	18.630	17.748	17.063	16.462	16.157	16.008
CFFF	1	1.0299	0.9263	0.8832	0.8526	0.8280	0.8135	0.8058
	2	2.3908	2.1528	2.0521	1.9787	1.9181	1.8839	1.8663
	3	6.0046	5.4091	5.1549	4.9675	4.8115	4.7255	4.6816
	4	7.6356	6.0506	5.7604	5.4439	5.0955	4.9709	4.9245
CCCC	1	9.6354	8.7011	8.2925	7.9756	7.6959	7.5521	7.4815
	2	18.305	16.567	15.783	15.147	14.563	14.282	14.149
	3	18.305	16.567	15.783	15.147	14.563	14.282	14.149
	4	25.506	23.111	22.014	21.099	20.247	19.849	19.666

Table 7
Variation of the frequency parameter $\omega^* = \omega a^2/h\sqrt{\rho_c/E_c}$ with the volume fraction exponent n for square Ti–6Al–4V/Aluminum oxide FG plates ($a/h = 10$)

Boundary condition	Mode	n						
		0	0.5	1	2	5	8	10
SSSS	1	5.6147	4.6754	4.2255	3.8897	3.6546	3.5435	3.4892
	2	13.420	11.257	10.114	9.2916	8.7480	8.4729	8.3417
	3	13.420	11.257	10.114	9.2916	8.7480	8.4729	8.3417
	4	20.484	17.2867	15.459	14.179	13.372	12.939	12.738
CFFF	1	1.0237	0.8463	0.7680	0.7075	0.6627	0.6428	0.6330
	2	2.4277	1.9981	1.8090	1.6615	1.5502	1.5019	1.4783
	3	6.0517	4.9987	4.5310	4.1634	3.8839	3.7635	3.7051
	4	6.6026	5.6426	5.1452	4.6267	4.0756	3.8816	3.8094
CCCC	1	9.7129	8.0712	7.3301	6.7304	6.2483	6.0444	5.9490
	2	18.666	15.543	14.115	12.929	11.939	11.531	11.347
	3	18.666	15.543	14.115	12.929	11.939	11.531	11.347
	4	26.152	21.801	19.795	18.106	16.669	16.087	15.827

Fig. 7 depicts the effects of the volume fraction exponent and length-to-thickness ratio on the fundamental natural frequency parameter of simply supported Al/ZrO$_2$ plates. It shows that, for plates with a certain volume fraction, the frequency rises as the length-to-thickness ratio increases up to around 20, but when it escalates further no evident frequency changes can be discerned. The same observations can be made from Fig. 8, which shows the impact of the volume fraction exponent and length-to-thickness ratio on the fundamental natural frequency parameters of fully clamped SUS304/Si$_3$N$_4$ plates. It is therefore concluded that the effects of the length-to-thickness ratio on the frequency of plates is independent of the variation in the volume fraction.

4.3. Skew plates

A skew plate with a skew angle α is shown in Fig. 9. Note that on the oblique edges of the skew plate, a transformation between the global and local displacements is needed to enforce of boundary condition. For a

Table 8
Variation of the frequency parameter $\omega^* = \omega a^2 / h \sqrt{\rho_c / E_c}$ with the volume fraction exponent n for square SUS304/Si$_3$N$_4$ FG plates $(a/h = 10)$

Boundary condition	Mode	n						
		0	0.5	1	2	5	8	10
SSSS	1	5.6148	3.8947	3.4242	3.0813	2.8058	2.7129	2.6768
	2	13.513	9.3645	8.2298	7.3991	6.7284	6.5032	6.4161
	3	13.513	9.3645	8.2298	7.3991	6.7284	6.5032	6.4161
	4	20.740	14.365	12.620	11.338	10.299	9.9517	9.8178
CFFF	1	1.0203	0.7059	0.6199	0.5576	0.5077	0.4907	0.4841
	2	2.4399	1.6681	1.4583	1.3065	1.1850	1.1434	1.1269
	3	6.0523	4.1666	3.6526	3.2790	2.9788	2.8766	2.8366
	4	6.6208	4.5977	4.0059	3.5409	3.1579	3.0436	3.0035
CCCC	1	9.6814	6.7091	5.8902	5.2874	4.8005	4.6389	4.5767
	2	18.627	12.896	11.314	10.142	9.1896	8.8760	8.7565
	3	18.627	12.896	11.314	10.142	9.1896	8.8760	8.7565
	4	26.114	18.069	15.846	14.192	12.846	12.404	12.236

Table 9
Effects of temperature on the frequency parameter $\omega^* = \omega a^2 / h \sqrt{\rho_c / E_c}$ for the square Ti–6Al–4V/Aluminum oxide FG plates $(a/h = 10)$

Boundary condition	n	Mode	T			
			100	400	700	1000
SSSS	0.5	1	4.6874	4.6492	4.5839	4.5066
	2	2	11.301	11.209	11.053	10.869
		1	3.9482	3.8647	3.7176	3.5312
		2	9.5006	9.2992	8.9473	8.5029
CCCC	0.5	1	8.1063	8.0407	7.9303	7.8001
	2	2	15.624	15.499	15.289	15.0434
		1	6.8101	6.6672	6.4189	6.1069
		2	13.094	12.819	12.348	11.759

certain point on the oblique edge, the displacement transformation is given by

$$
\begin{Bmatrix} u \\ v \\ w \\ \theta_x \\ \theta_y \end{Bmatrix} = \begin{bmatrix} \sin\alpha & -\cos\alpha & 0 & 0 & 0 \\ \cos\alpha & \sin\alpha & 0 & 0 & 0 \\ 0 & 0 & 1 & 0 & 0 \\ 0 & 0 & 0 & \sin\alpha & -\cos\alpha \\ 0 & 0 & 0 & \cos\alpha & \sin\alpha \end{bmatrix} \begin{Bmatrix} u' \\ v' \\ w' \\ \theta'_x \\ \theta'_y \end{Bmatrix},
\tag{43}
$$

where u', v', w', θ'_x, and θ'_y are the displacements in the local coordinate system. For the nodes that are not located on the oblique edges, the transformation matrix is a unit matrix.

In this section, isotropic skew plates are considered first. A regular nodal distribution of 17×17 is used for the skew plate analysis, and the following geometry properties are adopted for the plates: $a/b = 1$, $a/h = 1000$ and $a/b = 5$, skew angle $\alpha = 15°$ and $45°$. The Poisson ratio is taken as 0.3, and the frequency parameter $\hat{\omega}$ is defined as

$$
\hat{\omega} = (\omega b^2 / \pi^2) \sqrt{\rho h / \check{D}}, \quad \check{D} = Eh^3 / 12(1 - v^2).
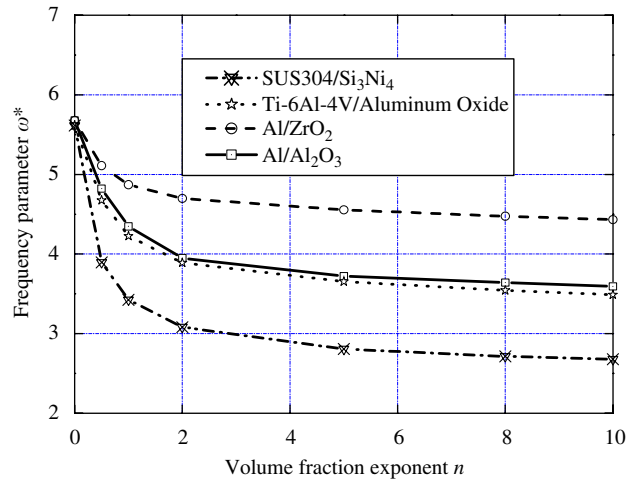\tag{44}
$$

Fig. 4. Variation of the fundamental natural frequency parameter with the volume fraction exponent for simply supported plates (SSSS).
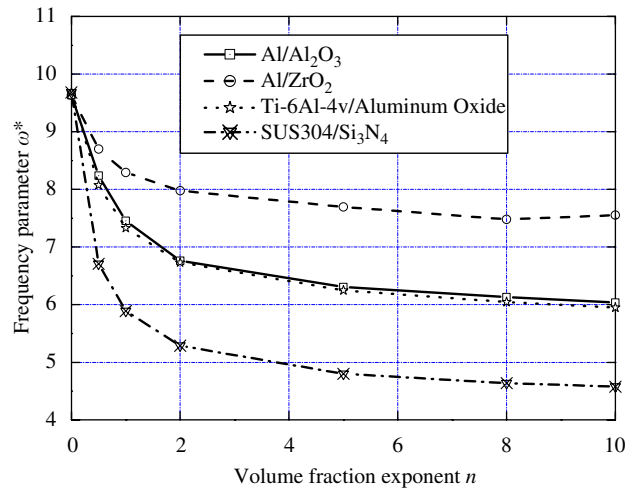

Fig. 5. Variation of the fundamental natural frequency parameter with the volume fraction exponent for fully clamped plates (CCCC).
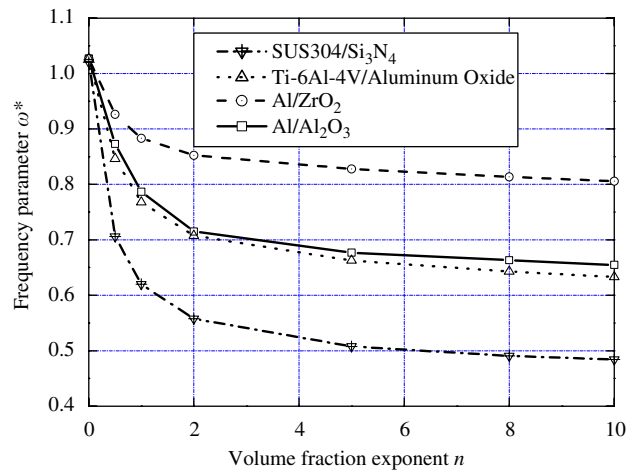

Fig. 6. Variation of the fundamental natural frequency parameter with the volume fraction exponent for plates with one edge clamped and the other three free (CFFF).
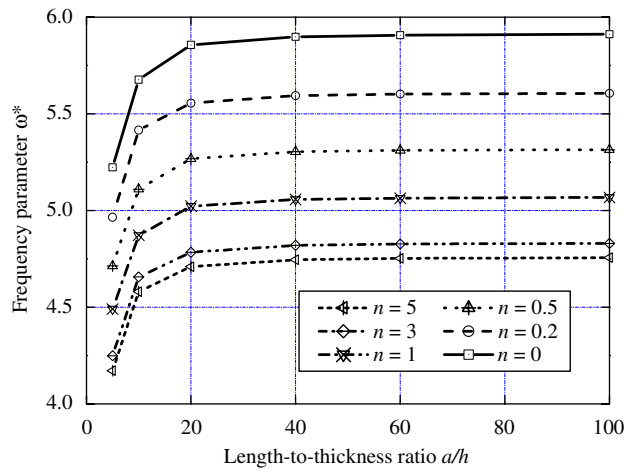
Fig. 7. Variation of the fundamental natural frequency parameter with the length-to-thickness ratio for simply supported Al/ZrO$_2$ plates.
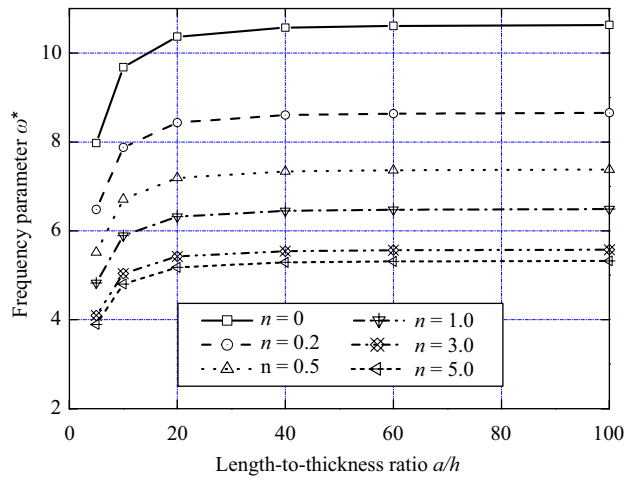

Fig. 8. Variation of the fundamental natural frequency parameter with the length-to-thickness ratio for fully clamped SUS304/Si$_3$N$_4$ plates.
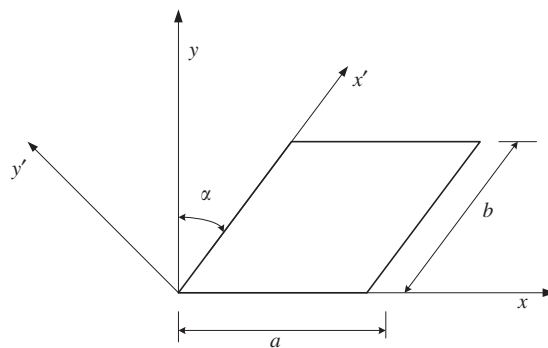

Fig. 9. Geometry of a skew plate.

Table 10 shows the frequencies of the first six modes for a simply supported skew plate ($\alpha = 15°$). For comparison, the solutions reported in the literature [40–43] are also provided. It can be seen that, for both a thin plate ($a/h = 1000$) and a relatively thick plate ($a/h = 5$), the results show very good agreement with the highly accurate solutions given by Liew et al. [41] and Huang et al. [40], and also compare well with the results produced by Woo et al. [42] and Raju and Hinton [43]. The frequencies for a fully clamped skew plate with $\alpha = 15°$ and a simply supported and a clamped skew plate with $\alpha = 45°$ are listed in Tables 11–13, respectively, and the same observations as those obtained from Table 10 can be made.

Tables 14 and 15 show the frequencies of the first four modes for simply supported and clamped functionally graded Al/ZrO$_2$ skew plates ($a/h = 10$, $a/b = 1$), respectively. The volume fraction exponent n varies between 0 and 3, and the skew angle ranges from $15°$ to $60°$. It is observed that, for plates with a fixed volume fraction exponent, the frequencies in all four modes increase with the rising skew angle, whereas for plates with a predetermined skew angle, the frequencies gradually drop as the volume fraction exponent increases.

Table 10

Comparison of the frequency parameter $\hat{\omega} = (\omega b^2/\pi^2)\sqrt{\rho h/\check{D}}$ for simply supported skew plates ($a/b = 1$, $v = 0.3$, $\alpha = 15°$)

h/b	Mode	$\hat{\omega}$				
		Present	Liew et al. [41]	Huang et al. [40]	Raju and Hinton [43]	Woo et al. [42]
0.001	1	2.1144	2.1147	2.1144	2.117	2.1149
	2	4.8632	4.8842	4.8842	4.903	4.8841
	3	5.6859	5.6856	5.6848	5.712	5.6872
	4	7.9776	8.0090	8.0087	8.069	8.0090
	5	10.5398	10.5372	10.5374	10.76	10.5377
	6	11.0665	11.0337	–	–	11.0277
0.2	1	1.8388	1.8560	–	1.860	1.8025
	2	3.7768	3.7856	–	3.803	3.7228
	3	4.2559	4.2763	–	4.300	4.2158
	4	5.5618	5.5784	–	5.617	5.4398
	5	6.8562	6.8385	–	6.947	6.7836
	6	7.0715	7.0702	–	–	7.0125

Table 11

Comparison of the frequency parameter $\hat{\omega} = (\omega b^2/\pi^2)\sqrt{\rho h/\check{D}}$ for clamped skew plates ($a/b = 1$, $v = 0.3$, $\alpha = 15°$)

h/b	Mode	$\hat{\omega}$				
		Present	Liew et al. [41]	Huang et al. [40]	Raju and Hinton [43]	Woo et al. [42]
0.001	1	3.8429	3.8691	3.8692	3.872	3.8679
	2	7.3569	7.3858	7.3859	7.421	7.3865
	3	8.3472	8.3708	8.3710	8.410	8.3757
	4	11.0521	11.1005	11.1009	11.180	11.1094
	5	14.1024	14.0806	14.0810	14.370	14.1151
	6	14.7446	14.7964	14.7070	–	14.7423
0.2	1	2.7953	2.8058	–	2.815	2.7882
	2	4.6246	4.6298	–	4.655	4.6108
	3	5.0938	5.0963	–	5.125	5.0869
	4	6.2998	6.3070	–	6.346	6.2708
	5	7.4235	7.4052	–	7.493	7.3881
	6	7.7388	7.7179	–		7.7050

Table 12

Comparison of the frequency parameter $\hat{\omega} = (\omega b^2 / \pi^2)\sqrt{\rho h / \breve{D}}$ for simply supported skew plates ($a/b = 1$, $v = 0.3$, $\alpha = 45°$)

h/b	Mode	$\hat{\omega}$				
		Present	Liew et al. [41]	Huang et al. [40]	Raju and Hinton [43]	Woo et al. [42]
0.001	1	3.5705	3.5800	3.5208	3.6648	3.5781
	2	6.6945	6.7153	6.7153	6.7632	6.7168
	3	10.1389	10.1756	10.1574	10.1979	10.1984
	4	10.9869	10.9754	10.8454	11.2467	11.0746
	5	14.2176	14.2662	14.2660	14.8334	14.3240
	6	17.0714	17.0518	–	–	17.1028
0.2	1	2.8037	2.9129	–	2.968	2.8799
	2	4.8528	4.8736	–	4.909	4.7955
	3	6.6434	6.6622	–	6.767	6.5052
	4	6.9295	7.0148	–	7.129	6.9893
	5	8.5063	8.4831	–	8.698	8.3615
	6	9.5509	9.5878	–	–	9.5051

Table 13

Comparison of the frequency parameter $\hat{\omega} = (\omega b^2 / \pi^2)\sqrt{\rho h / \breve{D}}$ for clamped skew plates ($a/b = 1$, $v = 0.3$, $\alpha = 45°$)

h/b	Mode	$\hat{\omega}$				
		Present	Liew et al. [41]	Huang et al. [40]	Raju and Hinton [43]	Woo et al. [42]
0.001	1	6.6123	6.6519	6.6510	6.665	6.6575
	2	10.7564	10.7898	10.7902	10.9	10.8259
	3	14.9769	15.0276	15.0271	15.36	15.2298
	4	15.9111	15.9342	15.9313	16.09	16.1277
	5	19.8852	19.9395	19.9373	20.77	20.5724
	6	23.3366	23.2526	23.2523	–	23.6702
0.2	1	4.1465	4.1590	–	4.178	4.1622
	2	5.8959	5.9021	–	5.947	5.9043
	3	7.5333	7.5422	–	7.628	7.4729
	4	7.7909	7.7907	–	7.849	7.8007
	5	9.2071	9.2159	–	9.374	9.2237
	6	10.1154	10.0921	–	–	10.1056

Figs. 10 and 11 describe the variation of the fundamental natural frequencies with the skew angle for simply supported and clamped plates. In addition to the observations made from Tables 14 and 15, it is discerned that the frequencies slowly improve as the skew angle increases from $0°$ to $30°$, with pronounced frequency increments occurring when the skew angle rises from $30°$ to $60°$. The frequency discrepancies among the plates with different volume fraction exponents also increase as the skew angle grows.

The frequencies in the first four modes for simply supported and clamped functionally graded SUS304/ Si_3N_4 skew plates ($a/h = 10$, $a/b = 1$) are presented in Tables 16 and 17, and similar frequency characteristics to those shown for Al/ZrO_2 plates are discerned.

4.4. Effects of the shear correction coefficient

The influence of different values of the shear correction coefficient on the frequency of the FG plates is investigated in this study. A variety of derivations for the shear correction coefficient has been proposed. A constant value of $K = 5/6$ is commonly used for the isotropic material. Timoshenko [44] presented a

Table 14
Variation of the frequency parameter $\omega^* = \omega a^2/h\sqrt{\rho_c/E_c}$ with the skew angle α for simply supported Al/ZrO$_2$ skew plates ($a/b = 1$, $a/h = 10$)

n	Mode	α			
		15°	30°	45°	60°
0	1	6.0071	7.0878	9.6709	16.597
	2	13.395	14.547	17.964	26.978
	3	15.3577	19.155	24.985	35.962
	4	20.979	22.152	27.259	45.463
0.2	1	5.7016	6.7283	9.1832	15.771
	2	12.724	13.820	17.071	25.661
	3	14.591	18.206	24.037	34.233
	4	19.943	21.061	25.928	43.308
0.5	1	5.4074	6.3816	8.7115	14.967
	2	12.073	13.114	16.202	24.366
	3	13.846	17.280	23.014	32.519
	4	18.929	19.993	24.618	41.158
1.0	1	5.1543	6.0827	8.3025	14.261
	2	11.505	12.496	15.437	23.209
	3	13.193	16.463	21.907	30.968
	4	18.034	19.046	23.449	39.188
3.0	1	4.9015	5.7817	7.8842	13.512
	2	10.913	11.849	14.622	21.927
	3	12.507	15.588	20.056	29.191
	4	17.067	18.019	22.153	36.859

Table 15
Variation of the frequency parameter $\omega^* = \omega a^2/h\sqrt{\rho_c/E_c}$ with the skew angle α for fully clamped Al/ZrO$_2$ skew plates ($a/b = 1$, $a/h = 10$)

| n	Mode	α			
		15°	30°	45°	60°
0	1	10.308	12.2116	16.635	27.502
	2	18.539	20.349	25.275	37.352
	3	20.750	25.452	33.377	46.061
	4	26.398	28.226	35.182	54.961
0.2	1	9.7996	11.6138	15.835	26.246
	2	17.645	19.375	24.086	35.656
	3	19.754	24.245	31.826	43.991
	4	25.144	26.893	33.554	52.506
0.5	1	9.3043	11.029	15.047	24.973
	2	16.765	18.413	22.902	33.944
	3	18.771	23.047	30.274	41.890
	4	23.899	25.568	31.921	50.002
1.0	1	8.8675	10.511	14.338	23.789
	2	15.973	17.542	21.816	32.325
	3	17.883	21.954	28.833	39.887
	4	22.765	24.354	30.399	47.587
3.0	1	8.3940	9.9388	13.523	22.315
	2	15.069	16.5315	20.509	30.238
	3	16.859	20.659	27.054	37.258
	4	21.429	22.902	28.505	44.042
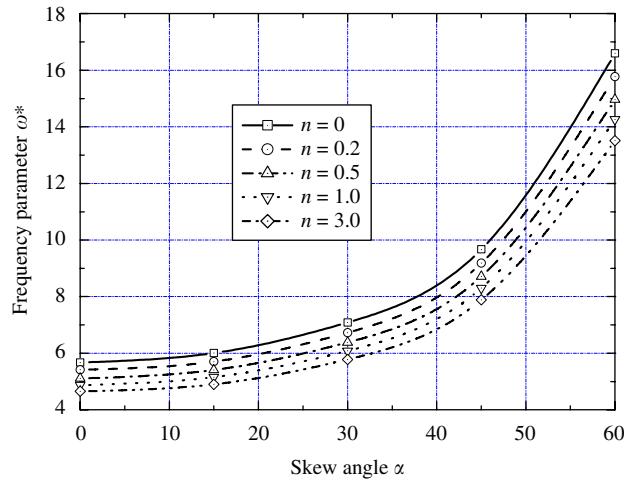
Fig. 10. Variation of the frequency parameter ω^* with the skew angle α for simply supported Al/ZrO$_2$ skew plates.
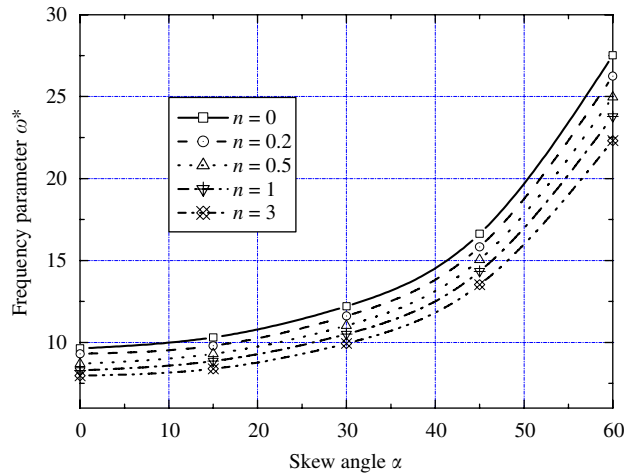

Fig. 11. Variation of the frequency parameter ω^* with the skew angle α for fully clamped Al/ZrO$_2$ skew plates.

shear correction coefficient that depends on the Poisson ratio v

$$K(v) = \frac{5 + 5v}{6 + 5v}.$$ (45)

A shear correction factor for FG plates was defined by Efraim and Eisenberger [20] as

$$K = \frac{5}{6 - (v_1 V_1 + v_2 V_2)},$$ (46)

where v_1 and v_2 represent the Poisson ratios for ceramic and metal, V_1 and V_2 denote the volume fractions for ceramic and metal in the entire cross section. Table 18 shows the effects of three different shear correction coefficients on the frequency of the Al/Al$_2$O$_3$ FG plates. The constant shear correction coefficient is termed as Sc-01, the factor given by Efraim and Eisenberger [20] is termed as Sc-02, and the shear coefficient proposed by Timoshenko [44] is termed as Sc-03. For the plate with $a/h = 5$, the results obtained from using shear correction coefficients Sc-02 and Sc-03 are more close to the solution produced from a higher-order deformation theory [21] than that derived from using a constant shear correction factor is. For the plate with $a/h = 10$, the difference among the results obtained from adopting three different types of shear factor is

Table 16
Variation of the frequency parameter $\omega^* = \omega a^2/h\sqrt{\rho_c/E_c}$ with the skew angle α for simply supported SUS304/Si$_3$N$_4$ skew plates ($a/b = 1$, $a/h = 10$)

n	Mode	α			
		15°	30°	45°	60°
0	1	5.9106	6.9723	9.5148	16.3609
	2	13.2202	14.3631	17.7541	26.7304
	3	15.1581	18.9198	25.5815	35.7040
	4	20.7447	21.9145	26.9757	45.4983
0.2	1	4.8097	5.6741	7.7430	13.3082
	2	10.7497	11.6779	14.4318	21.7179
	3	12.3255	15.3821	20.8077	28.9991
	4	16.8611	17.8103	21.9230	36.7314
0.5	1	4.1002	4.8376	6.6021	11.3456
	2	9.1608	9.9514	12.2969	18.5011
	3	10.5043	13.1092	17.6516	24.6997
	4	14.3669	15.1749	18.6809	31.2779
1.0	1	3.6049	4.2534	5.8049	9.9728
	2	8.0505	8.7447	10.8042	16.2479
	3	9.2312	11.5192	15.3314	21.6829
	4	12.6218	13.3307	16.4099	27.4443
3.0	1	3.0949	3.6512	4.9809	8.5468
	2	6.9011	7.4945	9.2536	13.8932
	3	7.9111	11.4097	12.7240	18.5130
	4	10.8054	13.1548	14.0359	23.3006

Table 17
Variation of the frequency parameter $\omega^* = \omega a^2/h\sqrt{\rho_c/E_c}$ with the skew angle α for clamped SUS304/Si$_3$N$_4$ skew plates ($a/b = 1$, $a/h = 10$)

n	Mode	α			
		15°	30°	45°	60°
0	1	10.1990	12.0959	16.5188	27.4788
	2	18.4045	20.2224	25.1807	37.4046
	3	20.6117	25.3277	33.3172	46.1961
	4	26.2651	28.1104	35.1335	55.199
0.2	1	8.2966	9.8388	13.4341	22.3412
	2	14.9637	16.4407	20.4684	30.3959
	3	16.7564	20.5866	27.0724	37.5292
	4	21.3455	22.8444	28.5481	44.8299
0.5	1	7.0674	8.3802	11.4394	19.0122
	2	12.7428	13.9989	17.4234	25.8586
	3	14.2686	17.5268	23.0405	31.9221
	4	18.1733	19.4473	24.2956	38.1218
1.0	1	6.2043	7.3546	10.0328	16.6493
	2	11.1789	12.2774	15.2706	22.6314
	3	12.5160	15.3673	20.1861	27.9302
	4	15.9364	17.0489	21.2831	33.3348
3.0	1	5.3044	6.2823	8.5527	14.1290
	2	9.5354	10.4634	12.9885	19.1696
	3	10.6715	13.0844	17.1479	23.6351
	4	13.5739	14.5099	18.0716	27.9680

Table 18
Effects of different shear correction coefficients on the natural frequency parameter $\bar{\omega} = \omega h \sqrt{\rho_c / E_c}$ for simply supported square Al/Al$_2$O$_3$ FG plates

a/h	Sc	n				
		0	0.5	1	4	10
5						
Present	Sc-01	0.2055	0.1757	0.1587	0.1356	0.1284
	Sc-02	0.2098	0.1790	0.1616	0.1383	0.1313
	Sc-03	0.2096	0.1788	0.1614	0.1382	0.1312
Matsunaga [21]		0.2121	0.1819	0.1640	0.1383	0.1306
10						
Present	Sc-01	0.05673	0.04818	0.04346	0.03757	0.03591
	Sc-02	0.05713	0.04849	0.04371	0.03781	0.03619
	Sc-03	0.05711	0.04847	0.04370	0.03779	0.03618
Matsunaga [21]		0.05777	0.04917	0.04426	0.03811	0.03642
20						
Present	Sc-01	0.01464	0.01241	0.01118	0.009702	0.009311
	Sc-02	0.01465	0.01241	0.01118	0.009706	0.009315
	Sc-03	0.01464	0.01241	0.01118	0.009705	0.009314

negligible. As the plate becomes thinner ($a/h = 20$), there is no discernible differences. It is concluded, therefore, for a relatively thick plate, the modified shear correction coefficients yield more accurate results than the constant factor does; for the plate with $a/h \geqslant 10$, the different shear correction factors have no pronounced effect on the solutions.

5. Conclusion

The free vibration analysis of FGPs is carried out using the element-free kp-Ritz method. A kernel particle estimate is employed to approximate the two-dimensional displacement field, and the first-order shear deformation plate theory is used to account for the transverse shear effect and rotary inertia. The elastic properties of FGPs are assumed to vary through the thickness according to a power law. The results derived with this method are compared with the solutions available in the literature to validate their accuracy. It is found that a volume fraction exponent that ranges between 0 and 5 has a significant influence on the frequency, but that the effects of the length-to-thickness ratio on the frequency of a plate are independent of the volume fraction. For a skew plate, a speeding frequency increment trend is observed at skew angles greater than 30°. It is found that the different values of shear correction coefficients have no pronounced effect on the frequency of FG plates with $a/h \geqslant 10$.

Acknowledgements

References

[1] M. Yamanouchi, T. Hirai, I. Shiota, Overall view of the P/M fabrication of functionally gradient materials, in: Proceedings of the First International Symposium on Functionally Gradient Materials, Sendai, Japan, 1990, pp. 59–64.
[2] N. Noda, Thermal stresses in functionally graded materials, Journal of Thermal Stresses 22 (1999) 477–512.

[3] G.N. Praveen, J.N. Reddy, Nonlinear transient thermo elastic analysis of functionally graded ceramic-metal plates, *International Journal of Solids and Structures* 35 (1998) 4457–4476.

[4] K.M. Liew, J. Yang, S. Kitipornchai, Thermal post-buckling of laminated plates comprising FGM with temperature-dependent properties, *Transactions of the ASME Journal of Applied Mechanics* 71 (2004) 839–850.

[5] K.M. Liew, J. Yang, S. Kitipornchai, Postbuckling of piezoelectric FGM plates subject to thermo-electro-mechanical loading, *International Journal of Solids and Structures* 40 (2003) 3869–3892.

[6] J.N. Reddy, Analysis of functionally graded plates, *International Journal for Numerical Methods in Engineering* 47 (2000) 663–684.

[7] J.N. Reddy, Z.Q. Cheng, Three-dimensional solutions of smart functionally graded plates, *Transactions of the ASME Journal of Applied Mechanics* 68 (2001) 234–241.

[8] K.M. Liew, X.Q. He, T. Ray, Computational intelligence in the optimal shape control of functionally graded smart plates, *Computer Methods in Applied Mechanics and Engineering* 193 (2004) 4475–4492.

[9] K.M. Liew, X.Q. He, S.A. Meguid, Optimal shape control of functionally graded smart plates using genetic algorithms, *Computational Mechanics* 33 (2004) 245–253.

[10] K.M. Liew, S. Sivashanker, X.Q. He, T.Y. Ng, Modelling and design of smart structures using functionally graded materials and piezoelectric sensor/actuator patches, *Smart Materials and Structures* 12 (2003) 647–655.

[11] K.M. Liew, S. Kitipornchai, X.Z. Zhang, C.W. Lim, Analysis of the thermal stress behavior of functionally graded hollow circular cylinders, *International Journal of Solids and Structures* 40 (2003) 2355–2380.

[12] H.L. Dai, X. Wang, Thermo-electro-elastic transient responses in piezoelectric hollow structures, *International Journal of Solids and Structures* 42 (2005) 1151–1171.

[13] X.L. Huang, S.H. Shen, Nonlinear vibration and dynamic response of functionally graded plates in thermal environments, *International Journal of Solids and Structures* 41 (2004) 2403–2427.

[14] J. Yang, S.H. Shen, Free vibration and parametric resonance of shear deformable functionally graded cylindrical panels, *Journal of Sound and Vibration* 261 (2003) 871–893.

[15] G.G. Sheng, X. Wang, Thermal vibration, buckling and dynamic stability of functionally graded cylindrical shells embedded in an elastic medium, *Journal of Reinforced Plastics and Composites* 27 (2008) 117–134.

[16] X.Q. He, T.Y. Ng, S. Sivashanker, K.M. Liew, Active control of FGM plates with integrated piezoelectric sensors and actuators, *International Journal of Solids and Structures* 38 (2001) 1641–1655.

[17] J. Yang, H.S. Shen, Vibration characteristics and transient response of shear-deformable functionally graded plates in thermal environments, *Journal of Sound and Vibration* 255 (2002) 579–602.

[18] S.S. Vel, R.C. Batra, Three-dimensional exact solutions for the vibration of functionally graded rectangular plate, *Journal of Sound and Vibration* 272 (2004) 703–730.

[19] K.M. Liew, X.Q. He, T.Y. Ng, S. Kitipornchai, Finite element piezothermoelasticity analysis and the active control of FGM plates with integrated piezoelectric sensors and actuators, *Computational Mechanics* 31 (2003) 350–358.

[20] E. Efraim, M. Eisenberger, Exact vibration analysis of variable thickness thick annular isotropic and FGM plates, *Journal of Sound and Vibration* 299 (2007) 720–738.

[21] H. Matsunaga, Free vibration and stability of functionally graded plates according to a 2-D higher-order deformation theory, *Composite Structures* 82 (2008) 499–512.

[22] P. Krysl, T. Belytschko, Analysis of thin plates by the element-free Galerkin method, *Computational Mechanics* 16 (1995) 1–10.

[23] P. Krysl, T. Belytschko, Analysis of thin shells by the element-free Galerkin method, *International Journal for Numerical Methods in Engineering* 33 (1996) 3057–3080.

[24] K.M. Liew, J. Ren, S. Kitipornchai, Analysis of the pseudoelastic behavior of a SMA beam by the element-free Galerkin method, *Engineering Analysis with Boundary Elements* 28 (2004) 497–507.

[25] K.M. Liew, L.X. Peng, S. Kitipornchai, Buckling analysis of corrugated plates using a mesh-free Galerkin method base on the first-order shear deformation theory, *Computational Mechanics* 38 (2006) 61–75.

[26] L.X. Peng, S. Kitipornchai, K.M. Liew, Free vibration analysis of folded plate structures by the FSDT mesh-free method, *Computational Mechanics* 39 (2007) 799–814.

[27] J.S. Chen, C. Pan, C.T. Wu, W.K. Liu, Reproducing kernel particle methods for large deformation analysis of nonlinear structures, *Computer Methods in Applied Mechanics and Engineering* 139 (1996) 195–227.

[28] W.K. Liu, S. Jun, Y.F. Zhang, Reproducing kernel particle methods, *International Journal for Numerical Methods in Engineering* 20 (1995) 1081–1106.

[29] K.M. Liew, J. Wang, T.Y. Ng, M.J. Tan, Free vibration and buckling analyses of shear deformable plates based on FSDT meshfree method, *Journal of Sound and Vibration* 276 (2004) 997–1017.

[30] S.N. Atluri, T.A. Zhu, A new meshless local Petrov–Galerkin (MLPG) approach, *Computational Mechanics* 22 (1998) 117–127.

[31] X. Zhao, K.M. Liew, T.Y. Ng, The element-free *kp*-Ritz method for free vibration analysis of conical shell panels, *Journal of Sound and Vibration* 295 (2006) 906–922.

[32] K.M. Liew, T.Y. Ng, X. Zhao, J.N. Reddy, Harmonic reproducing kernel particle method for free vibration analysis of rotating cylindrical shells, *Computer Methods in Applied Mechanics and Engineering* 191 (2002) 4141–4157.

[33] X. Zhao, K.M. Liew, T.Y. Ng, Vibration analysis of laminated composite cylindrical panels via a mesh-free approach, *International Journal of Solids and Structures* 40 (2003) 161–180.

[34] K.M. Liew, J. Wang, M.J. Tan, S. Rajendran, Postbuckling analysis of laminated composite plates using the mesh-free *kp*-Ritz method, *Computer Methods in Applied Mechanics and Engineering* 195 (2006) 551–570.

[35] Y.S. Touloukian, *Thermophysical Properties of High Temperature Solid Materials*, McMillan, New York, 1967.

[36] J.N. Reddy, C.D. Chin, Thermo-mechanical analysis of functionally graded cylinders and plates, *Journal of Thermal Stresses* 21 (1998) 593–626.

[37] J.N. Reddy, *Mechanics of Laminated Composite Plates—Theory and Analysis*, CRC Press, New York, 1997.

[38] T. Belytschko, Y.Y. Lu, L. Gu, Element-free Galerkin method, *International Journal for Numerical Methods in Engineering* 20 (1995) 1081–1106.

[39] R.E.D. Bishop, *The Mechanics of Vibration*, Cambridge University Press, New York, 1979.

[40] C.S. Huang, O.G. McGee, A.W. Leissa, J.W. Kim, Accurate vibration analysis of simply supported rhombic plates by considering stress singularities, *Journal of Vibration and Acoustics* 117 (1995) 245–251.

[41] K.M. Liew, Y. Xiang, S. Kitipornchai, C.M. Wang, Vibration of thick plates based on Mindlin shear deformation plate theory, *Journal of Sound and Vibration* 168 (1993) 39–69.

[42] K.S. Woo, C.H. Hong, P.K. Basu, C.G. Seo, Free vibration of skew Mindlin plates by *p*-version of F.E.M., *Journal of Sound and Vibration* 268 (2003) 637–656.

[43] K.K. Raju, E. Hinton, Natural frequencies and modes of rhombic Mindlin plates, *Earthquake Engineering and Structural Dynamics* 8 (1980) 55–62.

[44] S.P. Timoshenko, On the transverse vibrations of bars of uniform cross-section, *Philosophical Magazine* 43 (1922) 125–131.